International Journal of Hydrogen Energy 56 (2024) 1139–1151

Contents lists available at ScienceDirect

International Journal of Hydrogen Energy

journal homepage: www.elsevier.com/locate/he

Trapping, hysteresis and Ostwald ripening in hydrogen storage: A pore-scale imaging study

Sepideh Goodarzi [a,*], Yihuai Zhang [a,b], Sajjad Foroughi [a], Branko Bijeljic [a], Martin J. Blunt [a]

[a] Department of Earth Science and Engineering, Imperial College, London, United Kingdom
[b] James Watt School of Engineering, University of Glasgow, Glasgow, United Kingdom

ARTICLE INFO

Dataset link: https://zenodo.org/records/10426407, https://github.com/ImperialCollegeLondon/porescale

Keywords:
Hydrogen storage
Gas trapping
Hysteresis
Ostwald ripening
X-ray imaging
Gas connectivity

ABSTRACT

Green hydrogen, produced from surplus electricity during peak production, can be injected into subsurface reservoirs and retrieved during high-demand periods. In this study, X-ray tomography was employed to examine hysteresis resulting from repeated hydrogen injection and withdrawal. An unsteady state experiment was performed to evaluate the distribution of hydrogen and brine after drainage and imbibition cycles: images of the pore-space configuration of fluids were taken immediately once injection had stopped and after waiting for a period of 16 h with no flow. A Bentheimer sandstone sample with a length of 60 mm and diameter of 12.8 mm was used, and hydrogen was injected at ambient temperature and a pore pressure of 1 MPa. The gas flow rate was decreased from 2 ml/min to 0.08 ml/min over three cycles of gas injection followed by water flooding, while the brine injection rate was kept constant. The results showed the presence of capillary pressure hysteresis and hydrogen migration through Ostwald ripening due to the diffusion of gas dissolved in the brine. These phenomena were characterized through analysis of interfacial curvature, area, connectivity and pore occupancy. The hydrogen tended to reside in the larger pore spaces, consistent with water-wet conditions. 16 h after flow had stopped, the hydrogen aggregated into larger ganglia with a single large connected ganglion dominating the volume. Moreover, the Euler characteristic decreased after 16 h, indicating an improvement in connectivity. The work implies that Ostwald ripening – mass transport of dissolved gas – leads to less hysteresis and better connectivity than would be assumed ignoring this effect, as done in assessments of hydrocarbon flow and trapping.

1. Introduction

To prevent dangerous climate change, it is crucial to shift towards low-carbon energy sources such as nuclear, solar, geothermal, wind, hydro, and biomass, combined with large-scale energy storage [1–3]. Renewable energy sources, such as solar and wind, have variable and unpredictable supply, requiring energy storage to match generation and consumption over both short and long periods. Energy storage can improve grid management and energy security, by balancing supply and demand facilitating the transition to a low-carbon economy [4,5].

Hydrogen is an attractive way to store energy with great potential to reduce reliance on non-renewable energy sources. It has numerous uses, including as a fuel for rockets, in boilers, for turbines and in fuel cells to generate electricity, as well as a feedstock for chemicals. Hydrogen can be stored as compressed gas, liquid hydrogen, adsorbed in metals and other materials, chemically bonded, and through oxidation with reactive metals [6,7]. For large-scale storage, only underground porous formations have the required capacity at a reasonable cost; however, further research is needed to fully evaluate the potential of specific sites and to develop safe and efficient storage methods [8].

An underground hydrogen storage project generally follows a cyclic operation with alternate periods of injection and withdrawal, depending on energy demand and the type of storage field used. The timing of injection and withdrawal can vary based on seasonal energy demand. These cycles involve primary drainage (hydrogen injection), secondary imbibition (hydrogen withdrawal), and secondary drainage (re-injection) followed by repeated withdrawal and injection. This is different from carbon dioxide storage, where only primary drainage (initial injection) and secondary imbibition (water displacement and capillary trapping) occur. The design and management of hydrogen storage require the consideration of hysteresis during multiple cycles of drainage and imbibition; this hysteresis controls the amount of hydrogen that can be recovered and how much is trapped in the pore space [1,7,9,10]. To thoroughly examine hysteresis, it is imperative to study multiple fluid injection cycles. The reason for this is that

* Corresponding author.
E-mail address: sepideh.goodarzi19@imperial.ac.uk (S. Goodarzi).

https://doi.org/10.1016/j.ijhydene.2023.12.029
Received 31 May 2023; Received in revised form 22 July 2023; Accepted 4 December 2023
Available online 3 January 2024

capillary pressure is not solely dependent on saturation, but also on the saturation history [11–13].

Another aspect of hydrogen storage is that the trapping and movement of hydrogen in its own phase might be affected by the transport of dissolved gas. In oilfield operations, it is commonly assumed that the dissolution of hydrocarbons is insignificant and that hysteresis is caused by the displacement between completely immiscible phases. This assumption is reflected in the use of hydrocarbon–water properties to describe hydrogen storage. However, both with hydrogen and carbon dioxide, this assumption is not valid [1,14,15].

Ostwald ripening impacts the distribution of fluids in porous media. Differences in local capillary pressure lead to differences in the concentration of dissolved gas from Henry's law. This in turn results in concentration gradients in the aqueous phase and diffusion of dissolved gas away from regions of high capillary pressure. Equilibrium is reached when the capillary pressure is uniform throughout the system. Several studies have investigated the effect of Ostwald ripening in porous media on the distribution of gases, such as carbon dioxide and air. For instance, Garing et al. [16] and De-Chalendar et al. [14] conducted experimental and theoretical studies, respectively, on the impact of Ostwald ripening on the pore-scale distribution of carbon dioxide. Blunt [17] quantified the configuration of gas in capillary–gravity equilibrium and estimated the time-scales to reach these equilibrium states. These studies have shown that significant rearrangement of gas can occur over time-scales of hours to months over length-scales of millimeters to centimeters. In regular pore networks, Ostwald ripening can lead to a more uniform distribution of trapped ganglia [18,19], but this may not be the case in heterogeneous porous rocks forming storage sites where multiple positions of equilibrium are possible [14]. Singh et al. [20,21] have presented a simulation methodology for Ostwald ripening in arbitrary pore geometries, exploring the influence of gas type, compressibility factor, and local capillary pressure. Their results highlight the significant impact of Ostwald ripening in heterogeneous or fractured porous structures, with implications for gas storage in the oil/water transition zone. Wang et al. [22] studied hydrogen transport in porous media under different wetting conditions using direct numerical simulation. Less water-wet conditions led to less snap-off and higher storage efficiency during drainage and larger hydrogen clusters during imbibition.

Recently, 3D X-ray microtomography has transformed our ability to understand flow in porous media. Advanced techniques and image processing algorithms can quantify pore-scale displacement processes, measure flow properties, and capture saturation below the image resolution [23,24]. Earlier studies using X-ray imaging focused on studying unsteady-state two-phase displacement, which provided valuable information on trapping and recovery efficiency for carbon dioxide storage and oil recovery applications, but it is not known if hydrogen behaves similarly in subsurface rocks [25–28]. Recent studies have used non-invasive high-resolution 3D X-ray imaging to study hydrogen trapped within rock that is otherwise saturated with water. These studies have revealed that hydrogen can be trapped to a significant degree, which may impact the effectiveness of storage and retrieval processes [29,30].

Several methods have been employed in recent studies to investigate hydrogen wettability, such as measuring contact angles, using the tilted plate technique [25], the captive bubble cell approach [26], direct X-ray imaging inside the rock [27] and in microfluidics devices [28]. These studies have found similar contact angles for hydrogen, methane, nitrogen, and carbon dioxide, despite the different multiphase flow parameters expected for hydrogen and water due to the interplay of viscous, capillary, and gravitational forces [28,31–33].

Limited studies have been conducted to observe the distribution of hydrogen at the pore scale. Higgs et al. [27] and Jha et al. [10] used X-ray imaging to examine the hydrogen saturation in initially brine-saturated sandstone. These studies found initial hydrogen saturations of up to 65% after primary drainage and a maximum residual saturation of 41% after imbibition. Boon and Hajibeygi [34] characterized hydrogen transport in geological porous, using medical X-ray CT scanning. At the centimeter scale, the interplay of viscous, capillary and viscous forces determines the amount of hydrogen trapping. Jangda et al. [30] studied the trapping of hydrogen after injecting brine that was both pre-equilibrated and not pre-equilibrated with hydrogen at high pressure and high temperature. They found an average contact angle of 54° and 53° when in contact with water after H_2-equilibrated and non-H_2-equilibrated brine injection, respectively. Moreover, there was a reduction in the residual saturation with non-H_2-equilibrated brine, indicating the dissolution of hydrogen may play a role in determining how much gaseous phase is present. Thaysan et al. [29] showed that during secondary imbibition, hydrogen recovery decreased with pressure, with lower recoveries at higher pressures. They suggested that future hydrogen storage operations in porous media should consider more shallow and lower-pressure sites to optimize recoverability. Zhang et al. [35] performed high-resolution 3D X-ray imaging to investigate the behavior of hydrogen injection and withdrawal in sandstone and compared the results to a similar experiment using nitrogen. They observed that hydrogen experiences less trapping due to lower initial saturation after drainage and a significant rearrangement of trapped hydrogen after imbibition, where many smaller ganglia of hydrogen disappeared while larger ones expanded, with no overall change in gas volume. In contrast, the fluid arrangement of nitrogen remained unchanged. They hypothesized that this rearrangement is caused by concentration gradients in the aqueous phase, Ostwald ripening, and provided an estimate of the time-scales for this effect to occur.

In this paper, we investigate the changes in ganglion size distribution, interfacial areas, and connectivity of hydrogen after repeated cycles of injection and withdrawal. Additionally, we study the effects of Ostwald ripening on these changes by taking images 16 h after each injection cycle had finished. Our study addresses the following scientific questions: (1) How does the trapping of hydrogen in porous media evolve during repeated injection and withdrawal cycles, and (2) how does Ostwald ripening influence these changes? We demonstrate that Ostwald ripening plays a significant role in improving the connectivity of the hydrogen, which can reduce the degree of hysteresis and enhance hydrogen storage capacity beyond what traditional hydrocarbon-based models would predict.

2. Materials and methods

2.1. Rock and fluid properties

We studied a sample of Bentheimer sandstone as it has an easily-resolved pore space and has been used as a benchmark in many flow and imaging studies. Bentheimer consists mostly of quartz (95%), with a small percentage of feldspar (4%), and trace amounts of fine clay (around 1%) [36]. The rock was drilled into a cylindrical sample 12.8 mm in diameter and approximately 60 mm in length. Previous studies have found a mean pore radius of approximately 30 μm, which means that the pore space can be easily resolved using X-ray imaging [37,38]. The total porosity of 22.6% was determined through image processing, and the absolute permeability was found to be 1.4 ± 0.1 D ($1.4 \times 10^{-12} \pm 0.1 \times 10^{-12}$ m^2), as measured under the experimental conditions.

Hydrogen was in the gaseous phase and to enhance the contrast between the phases, Potassium Iodide (KI) was added to deionized water, a process known as doping. Brine solutions were created by dissolving different weight percentages of KI in deionized water. A mixture of brine solution and several small pieces of the Bentheimer sample were imaged. The greatest contrast between the phases was when KI was dissolved in deionized water with a weight percentage of 3.5%.

During the experiment, the pore pressure and confining pressure were maintained at a constant level of 1 MPa and 2 MPa, respectively, and the temperature was kept at 25 °C. Under these conditions, the dynamic viscosity of gas was 8.94×10^{-6} Pa s [39] with an interfacial tension of $\sigma_{gw} = 7.29 \times 10^{-2}$ N m^{-1} with brine [35].

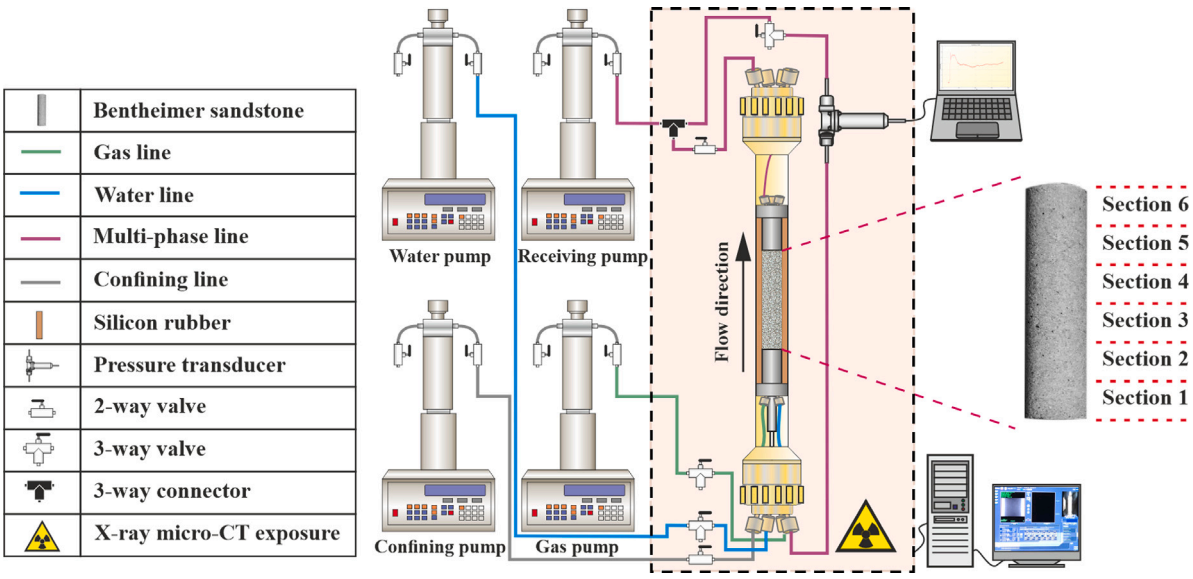

Fig. 1. A schematic diagram for the two-phase hydrogen–brine experiment conducted with the X-ray microtomography scanner (micro-CT). The arrangement of the core holder, pumps, flow lines, valves, and pressure transducer used in the experiment are represented in the diagram. The micro-CT enclosure is indicated by the black dashed line.

Table 1
Capillary numbers, $Ca = \mu q/\sigma$, where μ is the viscosity of the injected fluid, σ is the interfacial tension and q is the Darcy velocity for the flooding cycles.

Cycle	Flooding step	$Ca_{[wg]}$	$Ca_{[gw]}$	Flow rate [ml min^{-1}]
1	1st Drainage	1.93×10^{-7}	-	2.00
2	2nd Drainage	3.86×10^{-8}	-	0.40
3	3rd Drainage	7.72×10^{-9}	-	0.08
1–3	Imbibition	-	5.79×10^{-9}	0.06

2.2. Experimental procedure

The experiment was conducted under capillary-controlled conditions and with unsteady-state flooding. The capillary number (Ca) is calculated from $Ca = \mu q / \sigma$, where μ is the viscosity of the displacing (injected) fluid, σ is the interfacial tension and q is the Darcy velocity of the injected phase [24], see Table 1. To investigate the saturation history, the flooding cycles were repeated three times, with the brine flow rate being held constant while the gas flow rate was varied. The protocol for initiating the unsteady-state two-phase flow micro-CT imaging experiment was as follows:

1. The sample was dried and then securely enclosed within a silicone rubber to prevent any interaction with the surrounding fluid. The top and bottom parts of the rubber were connected to the production and injection pieces, respectively, as shown in Fig. 1.
2. The coreholder was then placed within the micro-CT apparatus (Zeiss Xradia 510 X-ray scanner), and relevant flowlines and pumps were employed to introduce the fluid phases and exert the necessary confining and back pressures, 1 MPa and 2 MPa, respectively. The pressure drop across the sample was accurately measured with a differential pressure transducer (Keller PD-33X), which was connected to the sample's inlet and outlet, with a precision of ±0.03 kPa. To minimize the risk of mixing hydrogen with air, the sample and lines were vacuumed for several hours to ensure a pure hydrogen environment.
3. The initial phase of the experiment involved scanning a dry sample. Subsequently, brine was introduced into the sample at a flow rate of 0.1 ml/min, starting from the bottom of the sample to achieve full saturation of the pore space. The brine flow rate was increased after 18 h by 0.5 ml/min and the pressure drop was continuously monitored until it stabilized. At this stage, the sample's absolute permeability was determined as 1.4 ± 0.1 D ($1.4 \times 10^{-12} \pm 0.1 \times 10^{-12}$ m^2) [24,40]. The low flow rate brine injection continued overnight at 0.05 ml/min and the brine-saturated sample was simultaneously scanned.
4. Three flooding cycles were conducted consecutively using the same procedure, with the gas flow rate being reduced. Each cycle began by introducing 10 pore volumes of gas at a specified flow rate. For cycle one the gas flow rate was 2 ml/min, for cycle two was 0.4 ml/min and for cycle 3 was 0.08 ml/min. The duration of gas injection varied across the cycles, with a time of 2 h for cycle 1, 8 h for cycle 2 and 12 h for cycle 3.
5. Once the gas injection (drainage) was completed after 2 h, the valve was closed, and the gas pump was switched off. A bottom-to-top scan of the sample was performed for 12 h, with each scan divided into six sections overlapping by 25%. Subsequently, after an additional 4 h had passed, making it a total of 16 h since the gas injection was stopped, images of sections 2 and 5 were captured over a period of four hours.
6. Ten pore volumes of brine were then injected (imbibition) at a steady flow rate of 0.06 ml/min for 6 h, followed by another 12 h bottom-to-top scan of the sample. After a further 4 h, images were taken of sections 2 and 5.
7. After completing the three cycles (steps 4–6), a scan of the entire sample was carried out 24 h later to evaluate the residual gas content.

2.3. Image processing and analysis

The imaging was performed using the Zeiss Xradia 510 X-ray scanner equipped with a flat panel detector. The exposure time was set to 1.2 s with a total of 3001 projections. The X-ray source was configured with a photon energy of 80 keV and a power of 7 W, with a 360° rotation angle of the sample. A single air filter was utilized between the source and sample. The detector provided three-dimensional images with a voxel size of 5.8 μm. During each scan, a total of six images were taken with a vertical overlap of 4 mm to ensure the entire length of the sample was captured. In total, the images covered 2069 voxels in the x-direction, 2187 voxels in the y-direction, and 9594 voxels in the z-direction. We will only discuss the arrangement of gas in the pore space

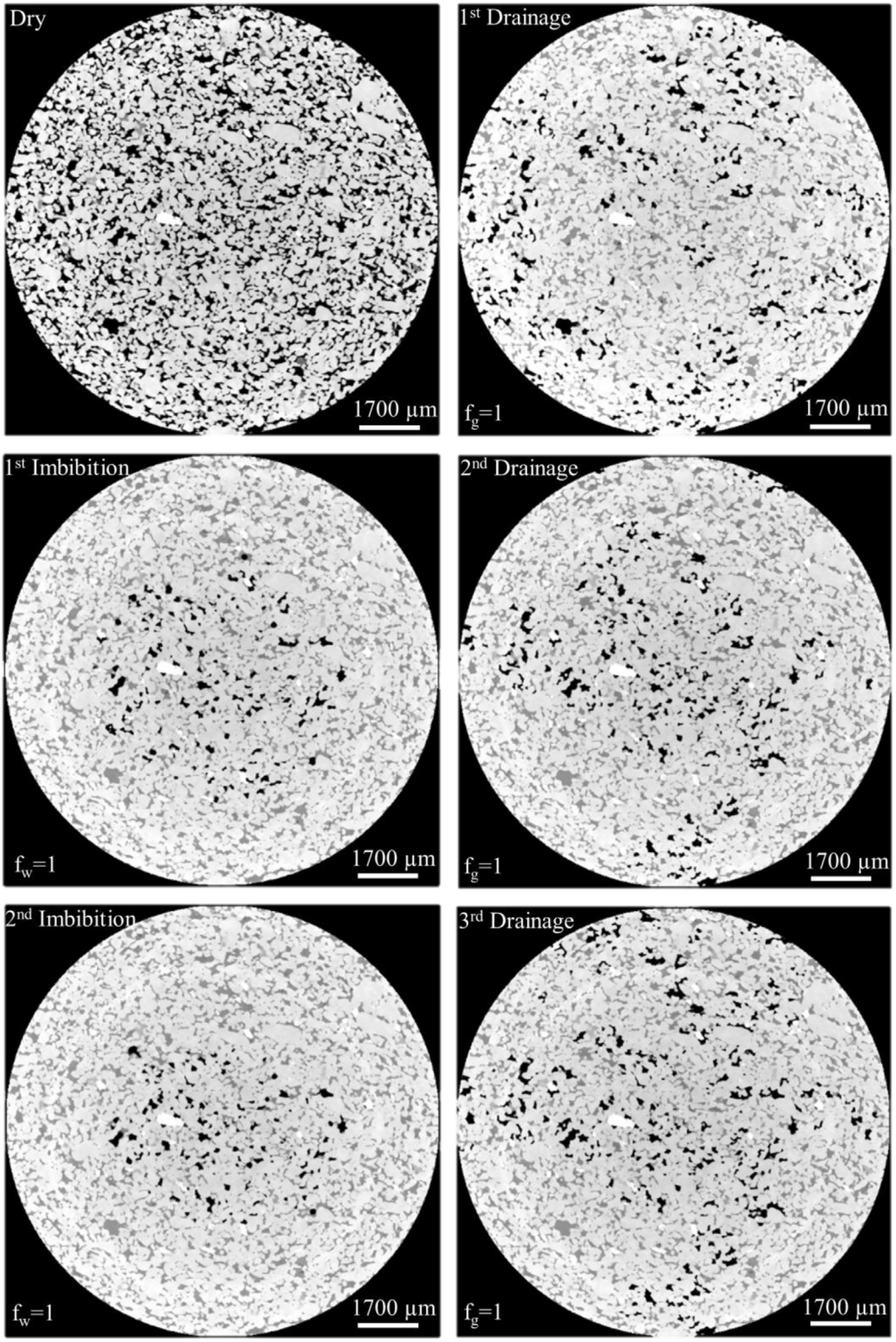

Fig. 2. Two-dimensional cross-sections of three-dimensional raw images of the Bentheimer sample before and after the three cycles of hydrogen and brine injection: the rock, gas, brine, and minerals are medium gray, black, light gray, and white, respectively.

after drainage and the first two imbibition cycles; after the third cycle all the hydrogen dissolved in the brine.

After acquiring the images, they were reconstructed, normalized, registered, and stitched together to obtain three-dimensional images of the rock and fluids at each cycle [41], see Fig. 2. We applied a non-local mean filter to reduce noise in our images [42]. Next, we used the watershed technique to segment different phases and extract specific measurements such as ganglion sizes, surface areas, and fluid saturation. This method allowed us to directly identify and separate the gas, brine, and rock phases in our images, see Fig. 3. An additional example of rearrangement in the gas phase, resulting in a change of connectivity for cycle two, is presented in the Supplementary Information Fig. S1.

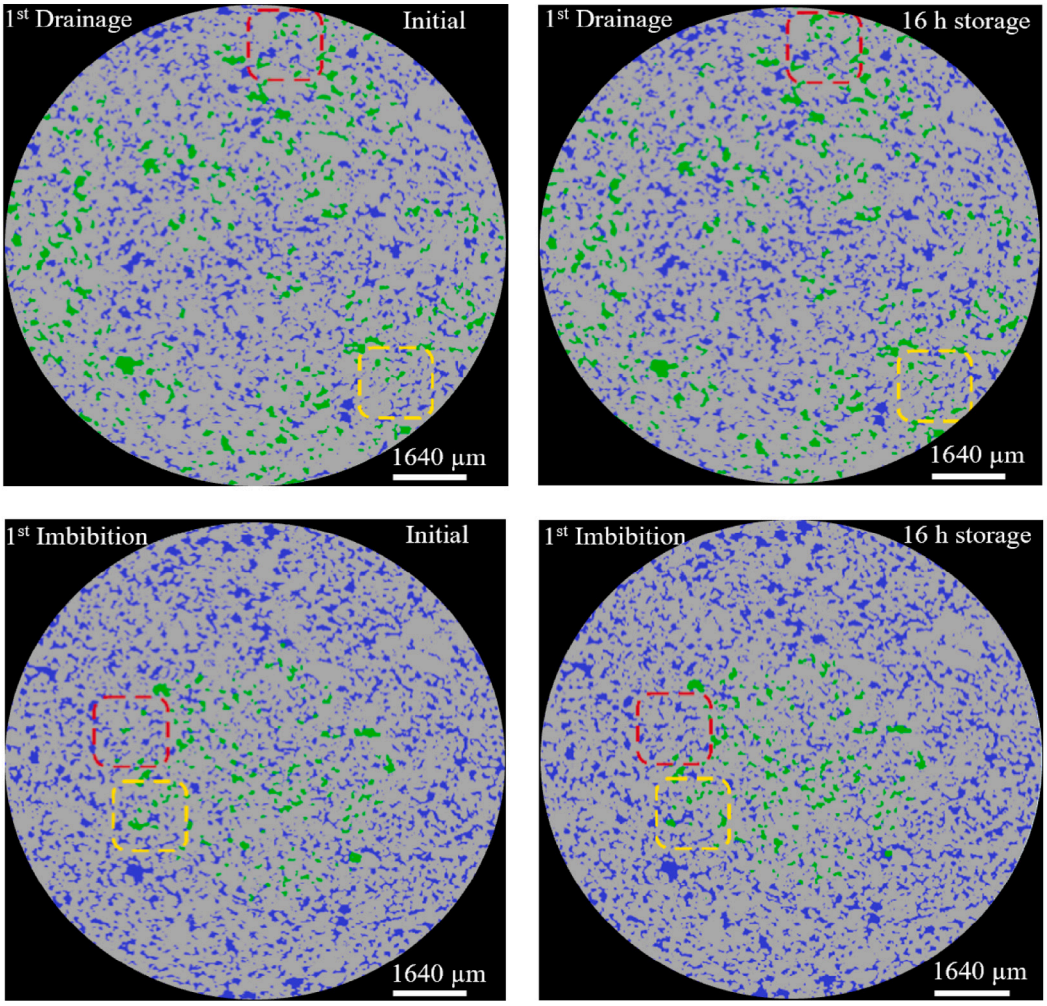

Fig. 3. Two-dimensional cross-sectional views of the segmented three-dimensional images showing the gas, brine, and rock phases in green, blue, and gray, respectively, for the initial state and after 16 h. Dashed lines represent locations where there have been rearrangements of the gas phase with a change in connectivity. (For interpretation of the references to color in this figure legend, the reader is referred to the web version of this article.)

3. Results and discussion

In this section, we present our pore-scale findings. In Section 3.1, we analyze discrete ganglia to confirm gas movement towards larger bubbles after an additional 16 h of waiting. Section 3.2 presents the gas saturation profiles measured across the sample during three cycles of gas injection and water flooding. Additionally, it includes a gas saturation profile for a sub-volume both in its initial state and after 16 h. In Section 3.3, we provide an analysis of the local capillary pressure after gas and water injection in three cycles. The measurements of fluid–fluid and fluid–solid specific interfacial area are plotted in Section 3.4. These results are presented in conjunction with the gas connectivity data discussed in Section 3.5 together with a quantification of the Péclet number. Lastly, in Section 3.6, we present the characterization of pore occupancy, including details on the distribution and arrangement of the fluids within the pore space.

3.1. Analysis of discrete ganglia

3D images of gas phase ganglia trapped inside the rock are shown in Fig. 4. These images were obtained for a sub-volume image size of $900 \times 900 \times 1373$ voxels located near the top of the sample (this is the central part of section 5, shown in Fig. 1). The trapped ganglia were imaged after injecting gas and water to the initial state and then waiting for 16 h for cycle one in Fig. 4. The trapped ganglia for cycle two are provided in the Supplementary Information S2. During the drainage stage, hydrogen injection followed by an additional 16-hour waiting period resulted in the formation of a single, large connected ganglion which is shown in green.

Additionally, we measured the ganglion size distributions in the sub-volume shown in Fig. 4, which revealed a significant movement of gas bubbles towards larger ganglia, spanning several pores, after gas injection and imbibition, see Fig. 5. It should be noted that the total gas volume remains approximately constant. Fig. 6 illustrates the cumulative volume distribution of ganglia. The graph highlights the phenomenon of bubble rearrangement, as smaller bubbles tend to disappear and contribute to the larger bubbles [17,20]. After 16 h, one large ganglion dominates the volume, as evidenced by the vertical portion in the cumulative curve at a large volume. This feature permits the withdrawal of hydrogen through a connected pathway, thus highlighting its potential significance in the remobilization of gas. This is aligned with the previous studies of gas–brine systems, where a significant rearrangement of the trapped gas was observed after brine injection [16,35].

3.2. Saturation profile

The cross-sectionally-averaged gas saturation along the entire sample length was measured, as depicted in Fig. 7. The flow rate used in the drainage cycles decreased from the first to the second to the

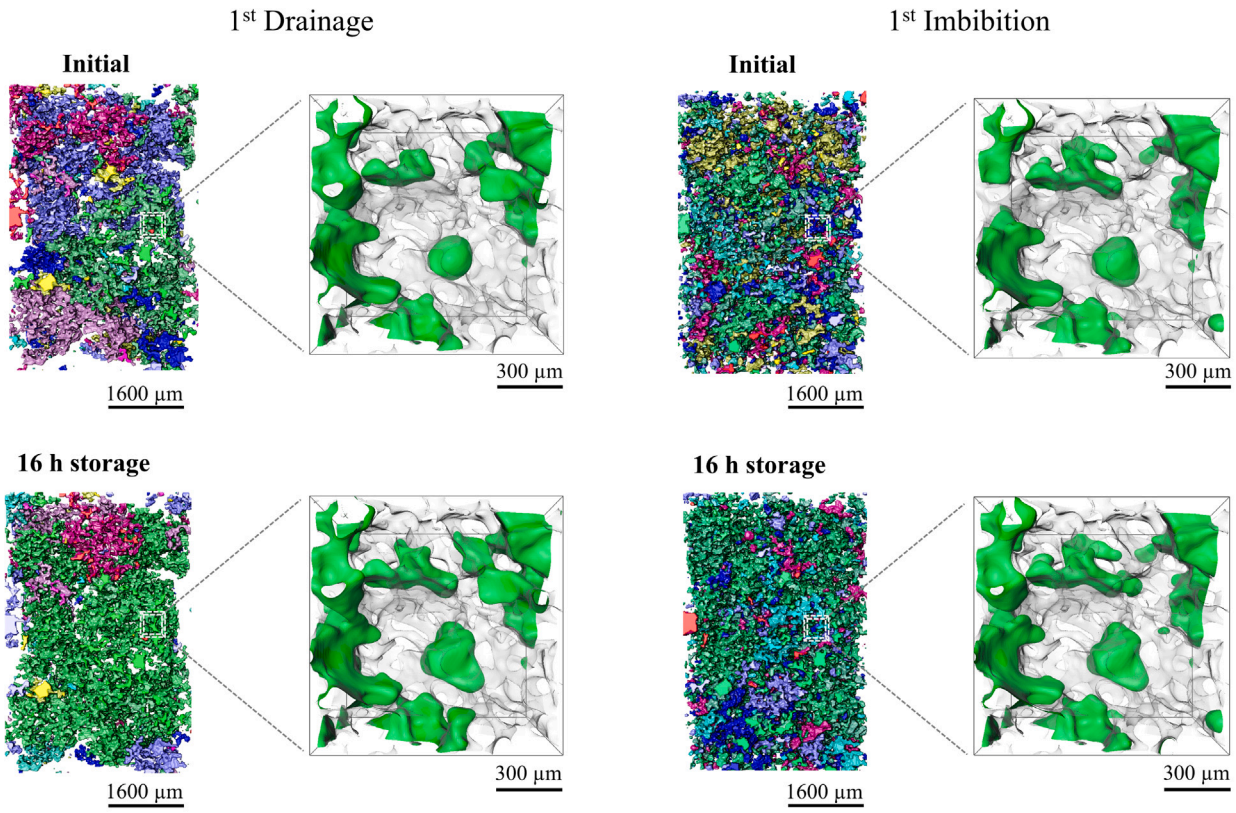

Fig. 4. 3D images of hydrogen in the pore space for cycle 1 of gas injection and water flooding. The different colors show discrete gas ganglia: after 16 h of storage these ganglia merge leading to better connectivity as indicated in the zoomed-in images on the right where the gas is shown in green. (For interpretation of the references to color in this figure legend, the reader is referred to the web version of this article.)

third cycle with a consequent decrease in hydrogen saturation. The maximum average gas saturation reached was approximately 30%. The residual hydrogen saturation was approximately 10%, but hydrogen was dissolved near the inlet and was completely dissolved in brine after the third imbibition cycle. We also plotted a gas saturation profile for a sub-volume located near the top of the sample (section 5, illustrated in Fig. 1). A comparison was made between the gas saturation during the initial cycle and after an additional 16-hour storage period, following three cycles of fluid injection, as shown in Fig. 8. The analysis indicated that gas saturation in the studied volume slightly increases after 16 h, suggesting that a small amount of gas may have migrated upward from lower sections of the sample.

3.3. Capillary pressure analysis

Fig. 9 presents a visual representation of the distribution of capillary pressure for all cycles on a sub-volume of 500 × 500 × 500 voxels (part of section 5, shown in Fig. 1). The capillary pressure for each stage was determined by calculating the average of the distribution of curvature and then applying the Young–Laplace equation [24]. The measurement of capillary pressure provides an average value and showed the capillary pressure after drainage is slightly higher than that after imbibition with no significant difference after the Ostwald ripening process. Nevertheless, the accuracy of the pressure measurements is limited due to the inherent uncertainty in the estimation of interfacial curvature from the pore-space images. The analysis of the capillary pressure data did not reveal any clear trends between the initial state and the 16-hour waiting period, as the results can fluctuate either upward or downward, with any changes potentially being drowned out by measurement errors.

3.4. Measurement of interfacial area

We conducted measurements to quantify the specific interfacial areas, defined as the area per unit volume (500 × 500 × 500 voxels, part of section 5, shown in Fig. 1). We determined the interfacial area between the water and gas, as well as between the fluids and the solid rock surface, both at the initial state and after a 16-hour waiting period, see Fig. 10. The results showed the sample is water-wet since the water–solid area is much higher than the gas–solid area: water preferentially contacts the solid surface. There is a tendency for the water–rock interfacial area to decrease during the waiting time, but the reduction is not significant. Conversely, the gas–rock area consistently increases. The gas–water interfacial area is much smaller and experiences a small decrease on waiting.

The increase in gas–solid interfacial area implies that the gas rearranges to contact more of the solid due to Ostwald ripening, possibly entering less water-wet regions of the pore space, or occupying larger ganglia with a greater contact area.

3.5. Fluid connectivity and Péclet number

Here, we took a closer look at the connectivity of fluids within the pore space, evaluating it qualitatively and quantitatively. We achieved this by isolating fluids from segmented images and giving each one a distinct color in the isolated phase, see Fig. 4. Table 2 provides a quantitative assessment of fluid connectivity from the Euler characteristic, measured in a sub-volume image size of 900 × 900 × 1373 voxels located near the top of the sample (section 5, shown in Fig. 1) as in the previous section.

The Euler characteristic, or Euler number, represents the number of objects (ganglia) in a phase, minus the number of redundant loops within those ganglia. A large positive Euler characteristic indicates that

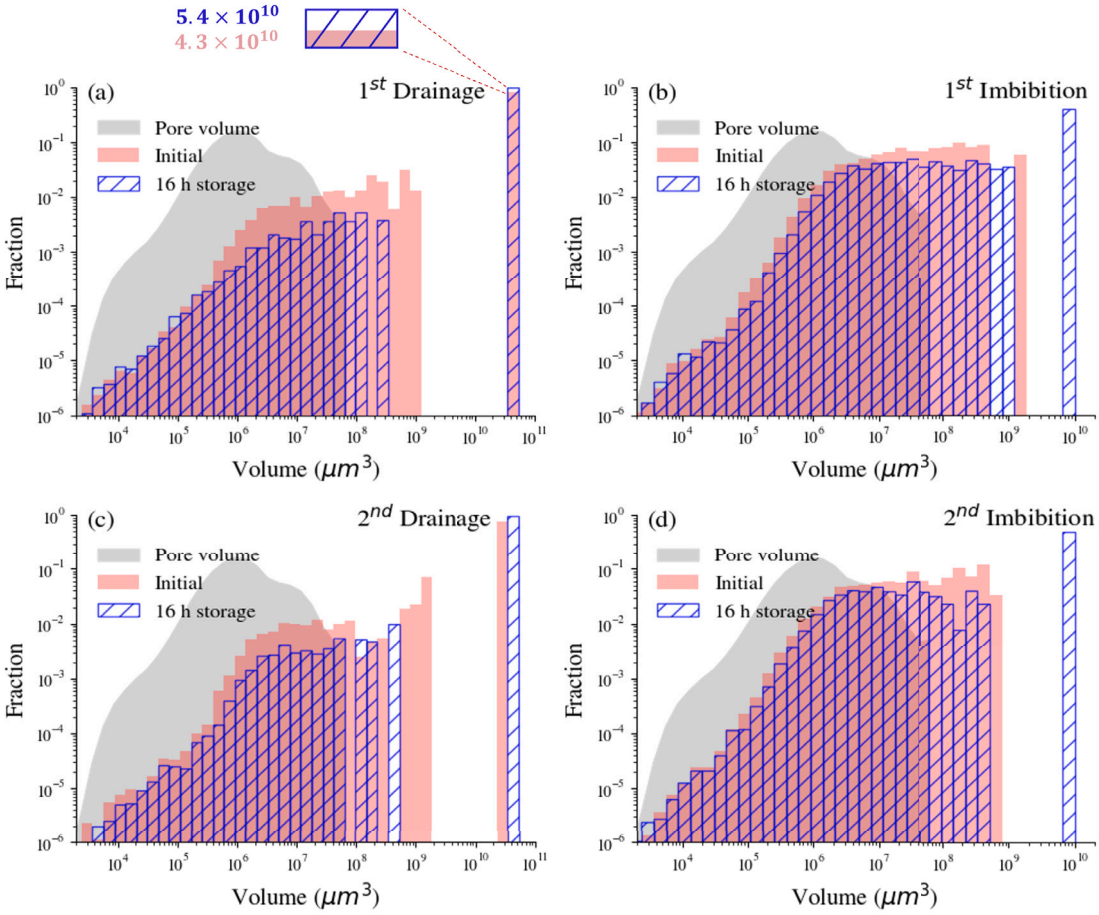

Fig. 5. The volume-weighted size distribution of ganglia is presented for the first (a,b) and second cycles (c,d) of gas and brine injection using a bin size that is uniform in logarithmic space. The gray-shaded area shows the volume distribution of all the pores.

Table 2
The Euler characteristic of a gas undergoing an unsteady-state two-phase experiment, both for the initial state and after 16 h, following three cycles of hydrogen and brine injection.

Normalized Euler characteristic [mm^{-3}]			
Cycle	Flooding step	Initial	16 h storage
1	1st Drainage	−5	−16
1	1st Drainage	18	10
2	2nd Drainage	−4	−8
2	2nd Imbibition	30	14
3	3rd Drainage	−3	−4

Note. The Euler characteristic was measured on segmented images of a sub-volume and normalized to the total volume.

the phase is trapped within numerous discrete ganglia, while a large negative Euler characteristic suggests a phase that is interconnected with many loops [43]. To ensure accuracy in our measurements, we have filtered out any features smaller than 10 voxels in size. As expected the Euler characteristic is negative after drainage, when the gas is well connected in the pore space, and positive after imbibition when the gas is trapped. In all cases, we see that after waiting 16 h the Euler characteristic decreases: this indicates an improvement in connectivity. This result is consistent with the formation and swelling of a single large connected ganglion shown in Fig. 6, and an overall tendency for the gas to congregate in fewer, larger ganglia as a result of Ostwald ripening, Fig. 5.

To understand the nature of displacement and fluid arrangement we also calculated the Péclet number, which is defined as the ratio of advective to diffusive transport of gas in a material [44,45]. The Péclet number is given by:

$$\mathrm{Pe} = \frac{q \cdot l}{D}, \tag{1}$$

where q is the Darcy velocity (volume of injected fluid flowing per unit time per unit area), l is the average distance between the centers of two neighboring pores, and D is the diffusion coefficient of the gas in brine, measured outside a porous medium. For the hydrogen–water system, D is 5.13×10^{-9} m^2/s [46] and l is 150 μm obtained from a pore-network analysis of the pore space described in the next section [47].

Eq. (1) compares the transport of hydrogen in its own phase by advection according to Darcy's law to the timescale for the diffusion-driven transport of hydrogen dissolved in the aqueous phase. The values are shown in Table 3. This analysis indicates that even during displacement, transport of dissolved gas can be significant in comparison with advective displacement. With the exception of the first drainage cycle, the time for hydrogen to move a pore length is shorter by diffusion through brine, than by displacement in its own phase. This indicates that in our experiments, with time-scales for displacement of order an hour and waiting times of 16 h, diffusive transport in the aqueous phase can play a significant role in the redistribution of the gas phase.

3.6. Pore and throat occupancy

Figs. 11 and 12 display the pore and throat size distributions, along with the volume-weighted fraction of gas-filled pore elements determined using the generalized pore network extraction tool. This method involves using the extracted pore network structures from

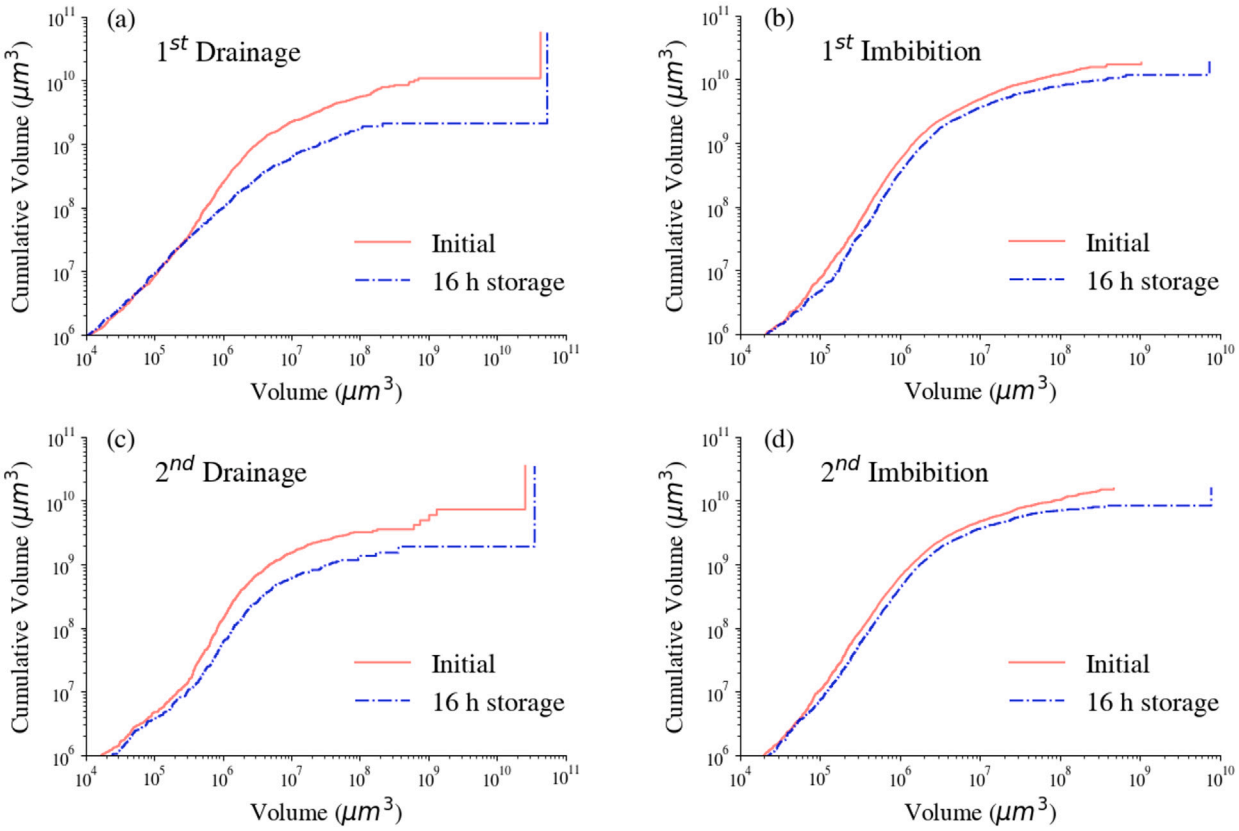

Fig. 6. The cumulative volume distribution of the ganglia near the top of the sample is shown for the first (a,b) and second cycles (c,d) of gas and brine injection. The vertical portion represents a single large ganglion that begins to dominate the volume after 16 h of storage.

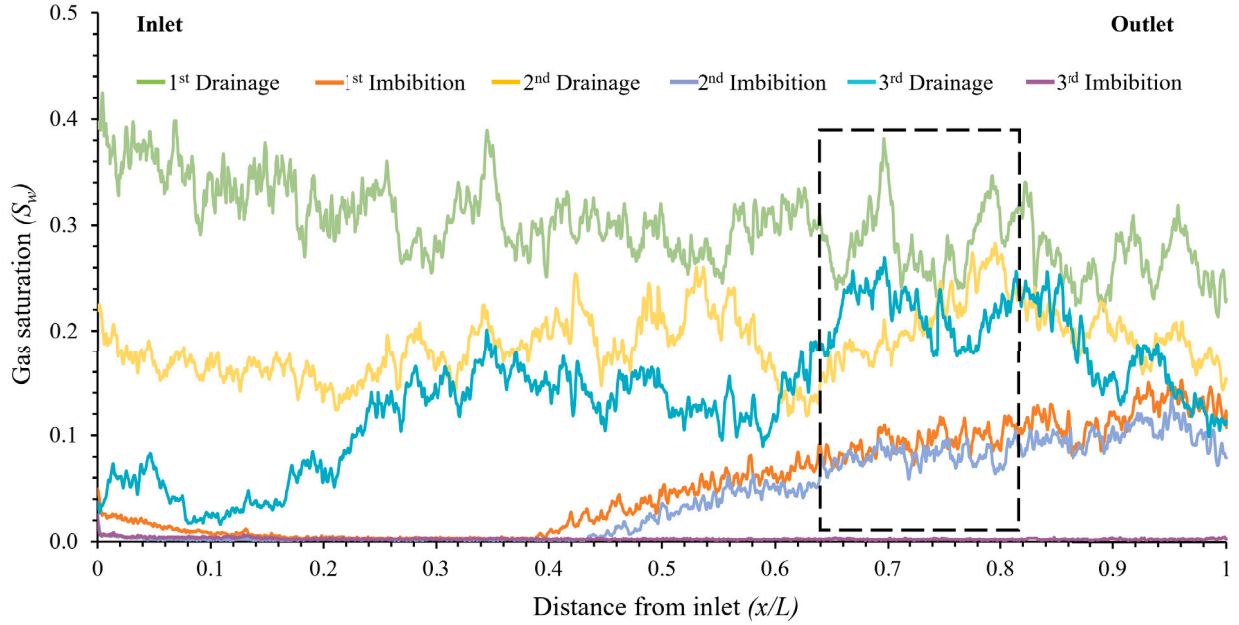

Fig. 7. Gas saturation profile measured from segmented images during three cycles of gas injection and water flooding at different gas flow rates and a constant water injection rate along the length of a Bentheimer sample. Gas is dissolved near the inlet after the water flooding stages. The subsection studied for further analysis is shown by the black dashed line.

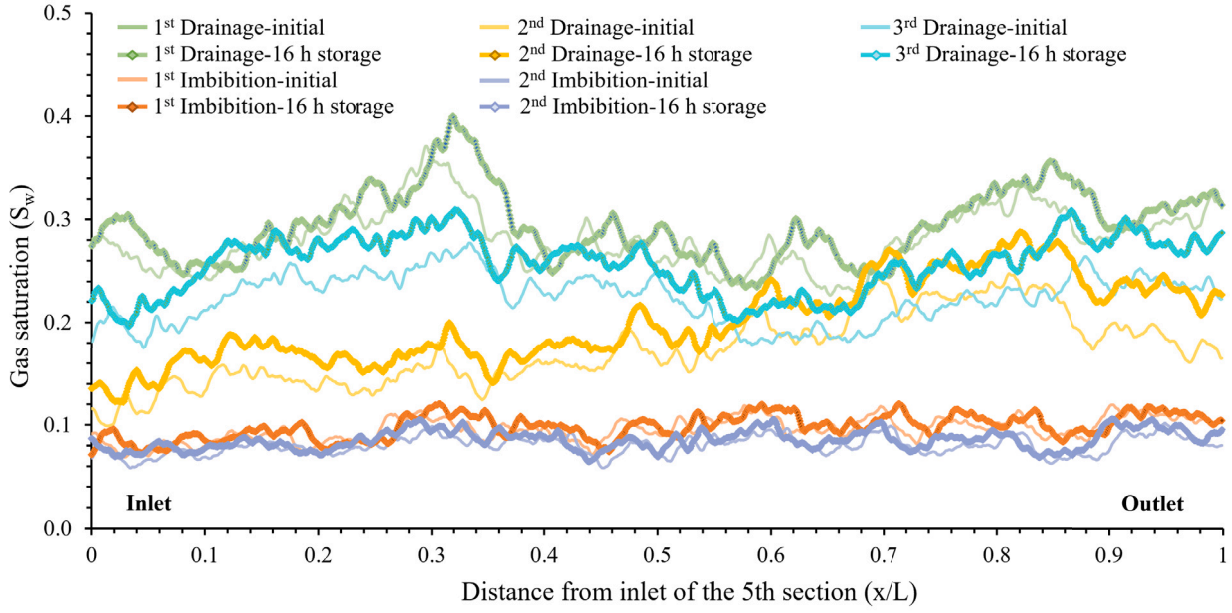

Fig. 8. The gas saturation profile of a sub-volume located near the top of the sample during three cycles of gas and water injection, including both the initial injection and after an additional 16-hour storage period. The region considered is indicated by the black dashed box in Fig. 7.

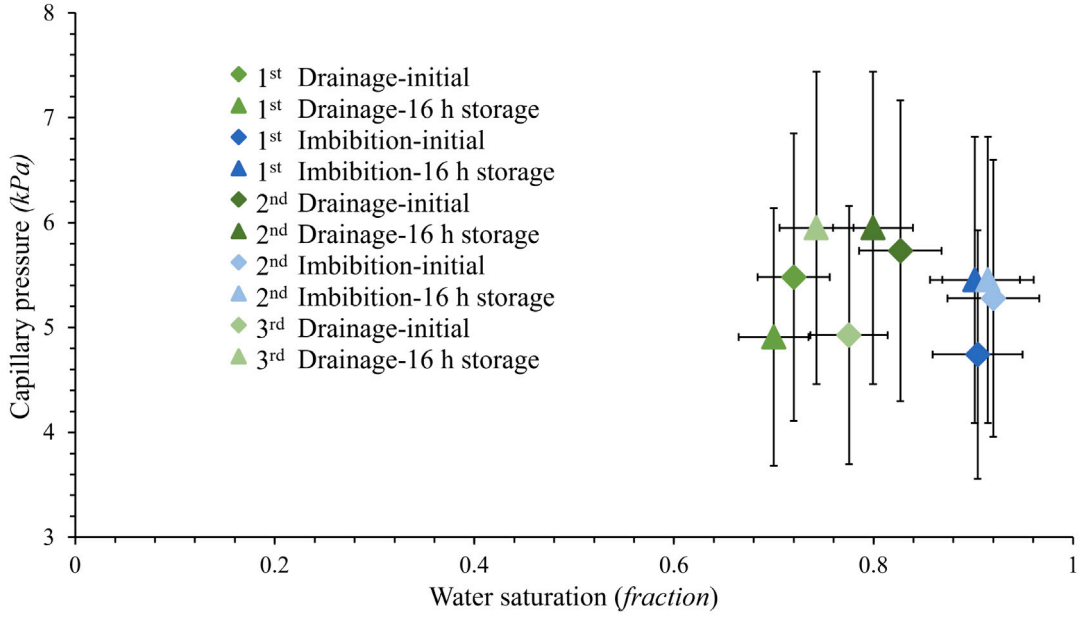

Fig. 9. Capillary pressure values as a function of water saturation are estimated from the mean interfacial curvature during both gas injection and water flooding steps.

the dry scan image as an image analysis tool, following Foroughi et al. [47,48]. Specifically, during pore network extraction from the dry scans, the inscribed spheres in each pore (a wide region in the void space) and throat (a restriction between pores) identified by the pore network extraction are calculated. These inscribed spheres were identified using the maximal ball method described by Dong and Blunt [49], and the generalized network extraction algorithm of Raeini et al. [50]. In pores, the largest spheres centered on each pore, which lie completely in the pore space, are identified. In throats, the largest spheres that can fit in the void space centered on the throat surface are identified. The inscribed spheres represent the local maxima (dilations) and minima (constrictions) in the distance map of the pore space, which are the locations where a non-wetting phase resides when it has just entered a pore or throat during drainage or the last location within

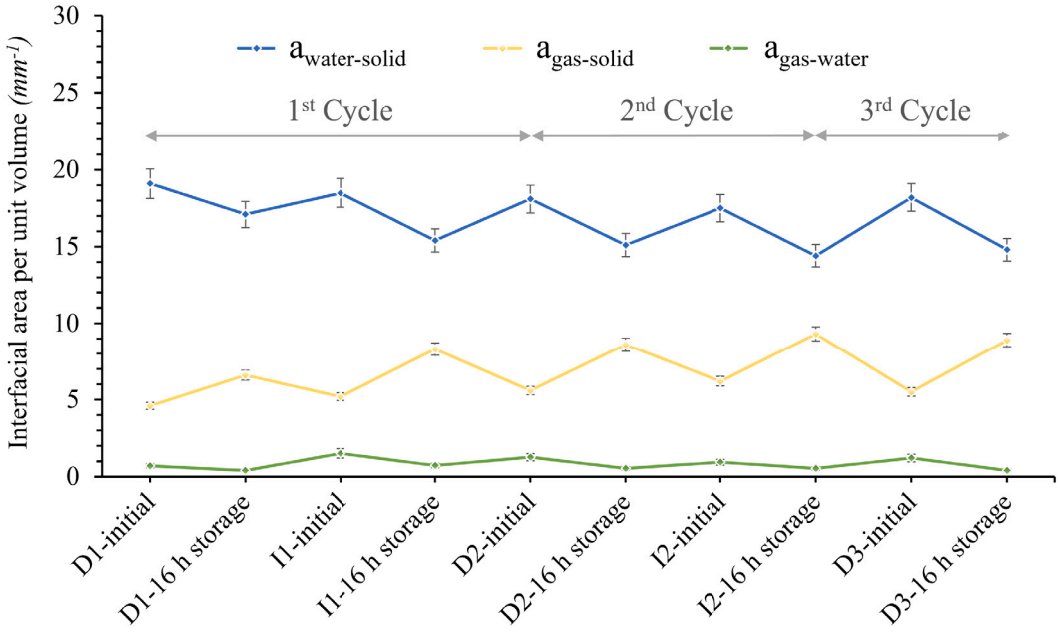

Fig. 10. The interfacial areas per unit volume for water–solid, gas–solid and gas–water in a voxel subvolume during three cycles of gas and water injection, including both the initial stage and after an additional 16-hour storage period. D stands for drainage and I for imbibition.

Table 3
The Péclet number, Eq. (1), of gas undergoing an unsteady-state two-phase experiment, following three cycles of hydrogen and brine injection.

Cycle	Flooding step	Darcy velocity [mm s^{-1}]	Capillary number Ca	Péclet number Pe
1	1st Drainage	0.260	1.93×10^{-7}	7.61
2	2nd Drainage	0.052	3.86×10^{-8}	1.52
3	3rd Drainage	0.010	7.72×10^{-9}	0.30
1–3	Imbibition	0.008	5.79×10^{-9}	0.23

a pore or throat where it can reside during imbibition. To determine which fluid resides in each inscribed sphere, we spatially registered the micro-CT images to each other so that the same voxel in each of the images corresponds to the same physical location in the sample. The mean square gray-scale value differences between the different images were minimized for this purpose. The images containing the inscribed spheres labeled with their corresponding pore number or throat number (as extracted from the dry scan) were then overlaid on each image acquired during the flow experiments. Based on the fluid phase which dominantly fills (more than 50%) the inscribed spheres of a pore or throat in the micro-CT image, we considered that phase as occupying the pore or throat.

Fig. 11 indicates the pore radii range from 20 to 100 μm, while Fig. 12 shows that throat radii range from 15 to 60 μm. After the first drainage, gas displaced brine from the larger and medium-sized pores, leaving most of the smaller pores filled with brine, consistent with the system being water-wet. The resolution of the images is, however, insufficient to measure contact angle directly. Little change in occupancy was seen after 16 h, implying that ganglion rearrangement is not principally the migration of gas into larger pores, but instead the aggregation of ganglia to occupy several connected pores. After imbibition, gas tended to be trapped in some of the larger and medium-sized pores, but again little change in occupancy was observed after 16 h. As shown in Fig. 12, we noticed a similar trend of gas filling in the throats.

4. Conclusions

We have studied the distribution of hydrogen in the pore space of a sandstone during repeated cycles of injection and withdrawal using high-resolution X-ray imaging. We imaged the sample every time either hydrogen or water was injected, and then again 16 h after the flow stopped.

The main conclusions of the work are as follows:

1. Hydrogen is the non-wetting phase and tends to occupy the larger regions of the pore space. It is trapped by the injection of water in the largest pores.
2. Even with no flow there is a significant rearrangement of the hydrogen within the pore space over length-scales of a centimeter and time-scales of 16 h. We hypothesize that this is caused by Ostwald ripening: the transfer of gas dissolved in the aqueous phase to equilibriate the local capillary pressure.
3. Ostwald ripening leads to the aggregation of hydrogen in larger ganglia with, in most cases, a single large ganglion dominating the volume.
4. The connectivity of the gas phase also increases after 16 h, as quantified by the Euler characteristic.

Our work implies that there may be less hysteresis in hydrogen storage than implied by the use of models based on hydrocarbons which ignore Ostwald ripening. This is favorable for hydrogen injection and withdrawal.

Future work could extend this study to other rock types, to study higher, more representative pressures to acquire higher-resolution images from which contact angle can be directly measured, and investigate the effect of pressure changes on the behavior [51]. Additionally, it would be valuable to inject brine that is pre-equilibrated with hydrogen to avoid the complicating effects of dissolution. The porous plate technique could be used to allow a higher initial hydrogen saturation to be reached in drainage. More accurate measurements of capillary pressure over a wide saturation range may allow the determination of a model of capillary pressure hysteresis applicable for hydrogen storage.

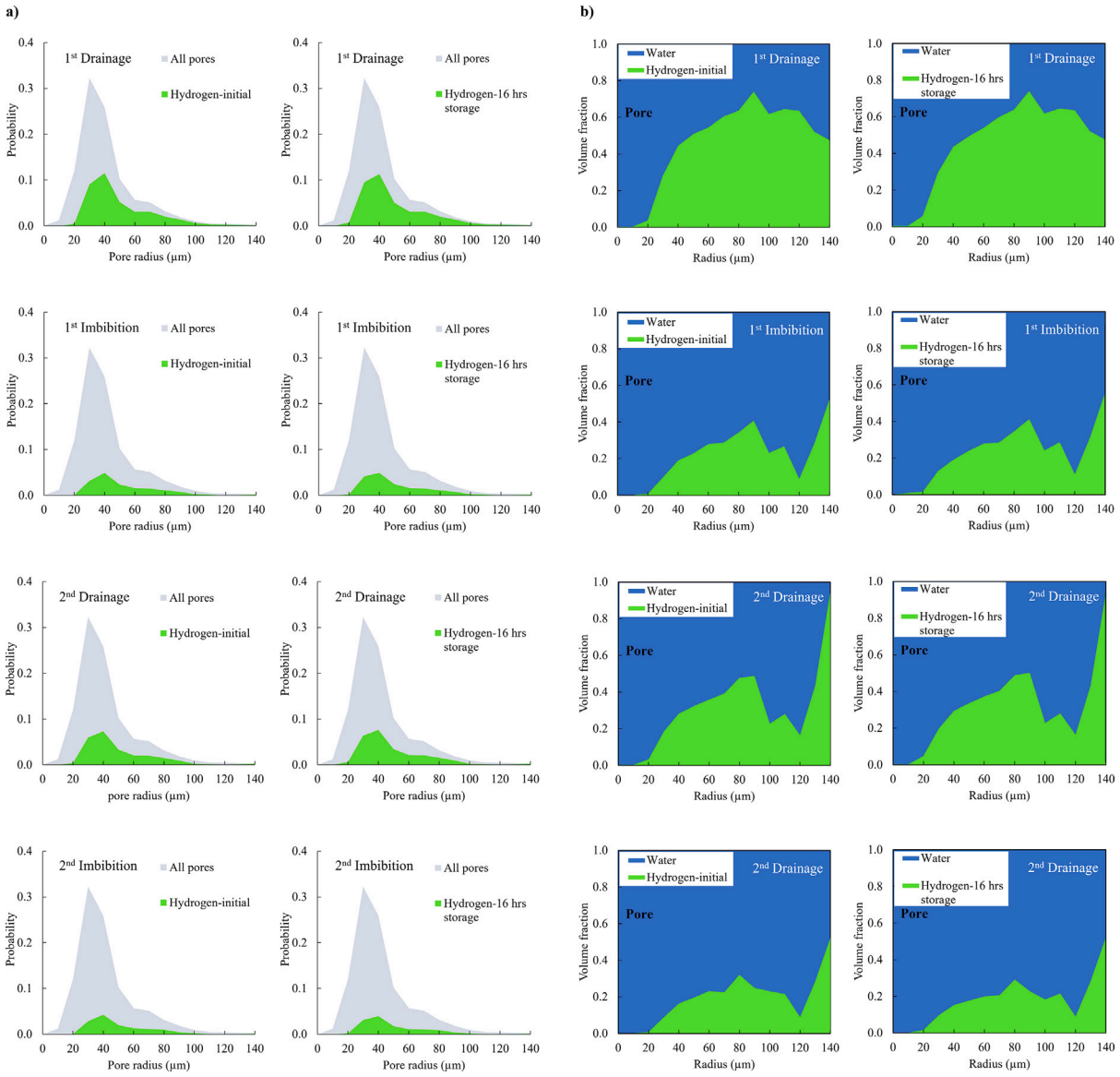

Fig. 11. (a) Probability histogram of the pore size distribution showing the gas-filled pore elements after gas injection and water flooding for both the initial and 16 h storage stages. The gray-shaded area shows the size distribution of all the pores. (b) Pore occupancy (volume fraction) as a function of pore radius representing the volume fraction occupied by gas (green) and water (blue). (For interpretation of the references to color in this figure legend, the reader is referred to the web version of this article.)

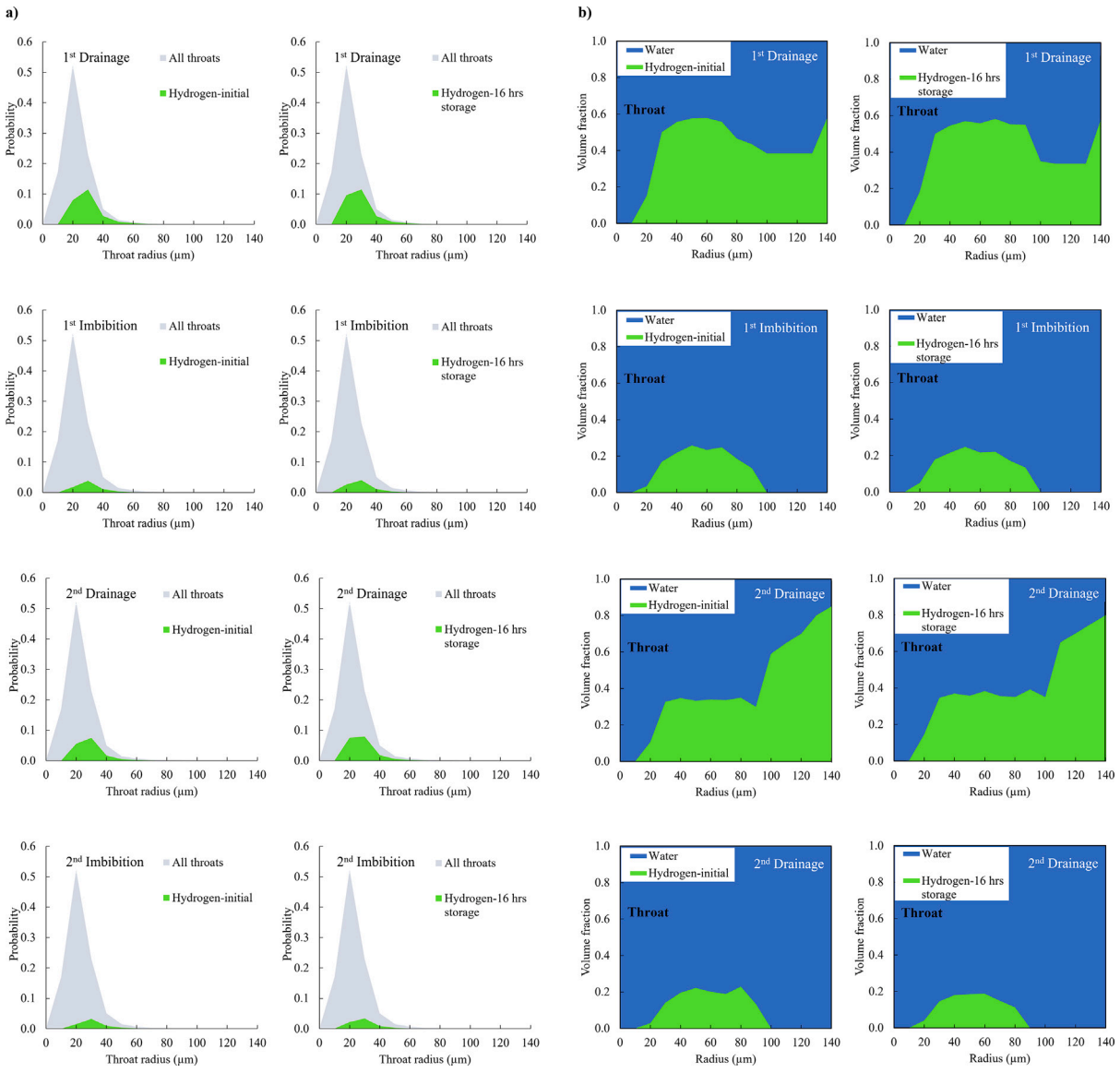

Fig. 12. (a) Probability histogram of the throat size distribution showing the gas-filled throat elements after gas injection and water flooding for both the initial and 16 h storage stages. The gray-shaded area shows the size distribution of all the throats. (b) Throat occupancy (volume fraction) as a function of throat radius representing the volume fraction occupied by gas (green) and water (blue). (For interpretation of the references to color in this figure legend, the reader is referred to the web version of this article.)

Declaration of competing interest

The authors declare that they have no known competing financial interests or personal relationships that could have appeared to influence the work reported in this paper.

Data availability

High-resolution versions of the referenced images in this study are available for download at https://zenodo.org/records/10426407 and the code used for the generation of pore and throat occupancy maps is accessible here https://github.com/ImperialCollegeLondon/porescale.

Acknowledgments

We thank Shell through the Digital Rocks program and EPSRC, United Kingdom grant number EP/V038044/1 INFUSE: Interface with the Future - Underpinning Science to Support the Energy Transition for funding this work. We are grateful to Dr. Steffen Berg for suggesting that we study Ostwald ripening and for useful discussions.

Appendix A. Supplementary data

Supplementary material related to this article can be found online at https://doi.org/10.1016/j.ijhydene.2023.12.029.

References

[1] Hematpur H, Abdollahi R, Rostami S, Haghighi M, Blunt MJ. Review of underground hydrogen storage: Concepts and challenges. Adv Geo-Energy Res 2023;7(2):111–31.
[2] Heinemann N, Alcalde J, Miocic JM, Hangx SJ, Kallmeyer J, Ostertag-Henning C, et al. Enabling large-scale hydrogen storage in porous media–the scientific challenges. Energy Environ Sci 2021;14(2):853–64.
[3] Mohan M, Sharma VK, Kumar EA, Gayathri V. Hydrogen storage in carbon materials—A review. Energy Storage 2019;1(2):e35.
[4] Rahman MM, Oni AO, Gemechu E, Kumar A. Assessment of energy storage technologies: A review. Energy Convers Manage 2020;223:113295.
[5] Tarkowski R. Underground hydrogen storage: Characteristics and prospects. Renew Sustain Energy Rev 2019;105:86–94.
[6] Usman MR. Hydrogen storage methods: Review and current status. Renew Sustain Energy Rev 2022;167:112743.
[7] Zivar D, Kumar S, Foroozesh J. Underground hydrogen storage: A comprehensive review. Int J Hydrogen Energy 2021;46(45):23436–62.

[8] Amirthan T, Perera M. Underground hydrogen storage in Australia: A review on the feasibility of geological sites. Int J Hydrogen Energy 2022.
[9] Lysyy M, Føyen T, Johannesen EB, Fernø M, Ersland G. Hydrogen relative permeability hysteresis in underground storage. Geophys Res Lett 2022;49(17):e2022GL100364.
[10] Jha NK, Al-Yaseri A, Ghasemi M, Al-Bayati D, Lebedev M, Sarmadivaleh M. Pore scale investigation of hydrogen injection in sandstone via X-ray micro-tomography. Int J Hydrogen Energy 2021;46(70):34822–9.
[11] Lenhard R, Parker J. Experimental validation of the theory of extending two-phase saturation-pressure relations to three-fluid phase systems for monotonic drainage paths. Water Resour Res 1988;24(3):373–80.
[12] Hassani V, Tjahjowidodo T, Do TN. A survey on hysteresis modeling, identification and control. Mech Syst Signal Process 2014;49(1–2):209–33.
[13] Teklu TW, Zhou Z, Li X, Abass H. Experimental investigation on permeability and porosity hysteresis in low-permeability formations. In: SPE low perm symposium, vol. 49. OnePetro; 2016, p. 1–30, 180226.
[14] de Chalendar JA, Garing C, Benson SM. Pore-scale modelling of ostwald ripening. J Fluid Mech 2018;835:363–92.
[15] Li X, Fan X. Effect of CO_2 phase on contact angle in oil-wet and water-wet pores. Int J Greenhouse Gas Control 2015;36:106–13.
[16] Garing C, de Chalendar JA, Voltolini M, Ajo-Franklin JB, Benson SM. Pore-scale capillary pressure analysis using multi-scale X-ray micromotography. Adv Water Resour 2017;104:223–41.
[17] Blunt MJ. Ostwald ripening and gravitational equilibrium: Implications for long-term subsurface gas storage. Phys Rev E 2022;106(4):045103.
[18] Xu K, Bonnecaze R, Balhoff M. Egalitarianism among bubbles in porous media: an ostwald ripening derived anticoarsening phenomenon. Phys Rev Lett 2017;119(26):264502.
[19] Joewondo N, Garbin V, Pini R. Experimental evidence of the effect of solute concentration on the collective evolution of bubbles in a regular pore-network. Chem Eng Res Des 2023;192:82–90.
[20] Singh D, Friis HA, Jettestuen E, Helland JO. A level set approach to ostwald ripening of trapped gas bubbles in porous media. Transp Porous Media 2022;145(2):441–74.
[21] Singh D, Friis HA, Jettestuen E, Helland JO. Pore-scale ostwald ripening of gas bubbles in the presence of oil and water in porous media. J Colloid Interface Sci 2023;647:331–43.
[22] Wang J, Yang Y, Cai S, Yao J, Xie Q. Pore-scale modelling on hydrogen transport in porous media: Implications for hydrogen storage in saline aquifers. Int J Hydrogen Energy 2023;48(37):13922–33.
[23] Saxena N, Hofmann R, Alpak FO, Dietderich J, Hunter S, Day-Stirrat RJ. Effect of image segmentation & voxel size on micro-CT computed effective transport & elastic properties. Mar Pet Geol 2017;86:972–90.
[24] Blunt MJ. Multiphase flow in permeable media: A pore-scale perspective. Cambridge University Press; 2017.
[25] Iglauer S, Ali M, Keshavarz A. Hydrogen wettability of sandstone reservoirs: implications for hydrogen geo-storage. Geophys Res Lett 2021;48(3):e2020GL090814.
[26] Hashemi L, Glerum W, Farajzadeh R, Hajibeygi H. Contact angle measurement for hydrogen/brine/sandstone system using captive-bubble method relevant for underground hydrogen storage. Adv Water Resour 2021;154:103964.
[27] Higgs S, Da Wang Y, Sun C, Ennis-King J, Jackson SJ, Armstrong RT, et al. In-situ hydrogen wettability characterisation for underground hydrogen storage. Int J Hydrogen Energy 2022;47(26):13062–75.
[28] van Rooijen W, Hashemi L, Boon M, Farajzadeh R, Hajibeygi H. Microfluidics-based analysis of dynamic contact angles relevant for underground hydrogen storage. Adv Water Resour 2022;104221.
[29] Thaysen EM, Butler IB, Hassanpouryouzband A, Freitas D, Alvarez-Borges F, Krevor S, et al. Pore-scale imaging of hydrogen displacement and trapping in porous media. Int J Hydrogen Energy 2022.
[30] Jangda Z, Menke H, Busch A, Geiger S, Bultreys T, Lewis H, et al. Pore-scale visualization of hydrogen storage in a sandstone at subsurface pressure and temperature conditions: Trapping, dissolution and wettability. J Colloid Interface Sci 2023;629:316–25.
[31] Lysyy M, Ersland G, Fernø M. Pore-scale dynamics for underground porous media hydrogen storage. Adv Water Resour 2022;163:104167.
[32] Arif M, Lebedev M, Barifcani A, Iglauer S. CO_2 Storage in carbonates: Wettability of calcite. Int J Greenhouse Gas Control 2017;62:113–21.
[33] Krevor S, Blunt MJ, Benson SM, Pentland CH, Reynolds C, Al-Menhali A, et al. Capillary trapping for geologic carbon dioxide storage–from pore scale physics to field scale implications. Int J Greenhouse Gas Control 2015;40:221–37.
[34] Boon M, Hajibeygi H. Experimental characterization of H_2/water multiphase flow in heterogeneous sandstone rock at the core scale relevant for underground hydrogen storage (UHS). Sci Rep 2022;12(1):14604.
[35] Zhang Y, Bijeljic B, Gao Y, Goodarzi S, Foroughi S, Blunt MJ. Pore-scale observations of hydrogen trapping and migration in porous rock: Demonstrating the effect of ostwald ripening. Geophys Res Lett 2023;50(7):e2022GL102383.
[36] Peksa AE, Wolf K-HA, Zitha PL. Bentheimer sandstone revisited for experimental purposes. Mar Pet Geol 2015;67:701–19.
[37] AbuAisha M, Billiotte J. A discussion on hydrogen migration in rock salt for tight underground storage with an insight into a laboratory setup. J Energy Storage 2021;38:102589.
[38] Alhosani A, Selem AM, Lin Q, Bijeljic B, Blunt MJ. Disconnected gas transport in steady-state three-phase flow. Water Resour Res 2021. e2021 WR031147.
[39] H_2Tools, hydrogen properties. 2015, https://h2tools.org/hyarc/hydrogen-properties. (1 March 2023).
[40] Gao Y, Lin Q, Bijeljic B, Blunt MJ. Pore-scale dynamics and the multiphase Darcy law. Phys Rev Fluids 2020;5(1):013801.
[41] Schlüter S, Sheppard A, Brown K, Wildenschild D. Image processing of multiphase images obtained via X-ray microtomography: a review. Water Resour Res 2014;50(4):3615–39.
[42] Buades A, Coll B, Morel J-M. A non-local algorithm for image denoising. In: 2005 IEEE computer society conference on computer vision and pattern recognition, vol. 2. Ieee; 2005, p. 60–5.
[43] Herring A, Robins V, Sheppard A. Topological persistence for relating microstructure and capillary fluid trapping in sandstones. Water Resour Res 2019;55(1):555–73.
[44] Gao Y, Georgiadis A, Brussee N, Coorn A, van Der Linde H, Dietderich J, et al. Capillarity and phase-mobility of a hydrocarbon gas-liquid system. Oil Gas Sci Technol Revue d'IFP Energies nouvelles 2021;76:43.
[45] Berg S, Gao Y, Georgiadis A, Brussee N, Coorn A, van der Linde H, et al. Determination of critical gas saturation by micro-CT. Petrophysics 2020;61(02):133–50.
[46] Hemme C, Van Berk W. Hydrogeochemical modeling to identify potential risks of underground hydrogen storage in depleted gas fields. Appl Sci 2018;8(11):2282.
[47] Foroughi S, Bijeljic B, Lin Q, Raeini AQ, Blunt MJ. Pore-by-pore modeling, analysis, and prediction of two-phase flow in mixed-wet rocks. Phys Rev E 2020;102(2):023302.
[48] Foroughi S, Bijeljic B, Blunt MJ. Pore-by-pore modelling, validation and prediction of waterflooding in oil-wet rocks using dynamic synchrotron data. Transp Porous Media 2021;138(2):285–308.
[49] Dong H, Blunt MJ. Pore-network extraction from micro-computerized-tomography images. Phys Rev E 2009;80(3):036307.
[50] Raeini AQ, Bijeljic B, Blunt MJ. Generalized network modeling: Network extraction as a coarse-scale discretization of the void space of porous media. Phys Rev E 2017;96(1):013312.
[51] Moghadasi R, Goodarzi S, Zhang Y, Bijeljic B, Blunt MJ, Niemi A. Pore-scale characterization of residual gas remobilization in CO_2 geological storage. Adv Water Resour 2023;104499.